Experimental Investigation of Flow Past a Square Cylinder at an Angle of Incidence

Sushanta Dutta[1]; P. K. Panigrahi[2]; and K. Muralidhar[3]

Abstract: Flow past a square cylinder placed at an angle to the incoming flow is experimentally investigated using particle image velocimetry, hot wire anemometry, and flow visualization. The Reynolds number based on cylinder size and the average incoming velocity is set equal to 410. Data for four cylinder orientations ($\theta=0$, 22.5, 30, and 45°) and two aspect ratios [AR=16 and 28] are reported. Results are presented in terms of drag coefficient, Strouhal number, time averaged velocity, stream traces, turbulence intensity, power spectra, and vorticity field. In addition, flow visualization images in the near wake of the cylinder are discussed. The shape and size of the recirculation bubble downstream of the cylinder are strong functions of orientation. A minimum in drag coefficient and maximum in Strouhal number is observed at a cylinder orientation of 22.5°. The v-velocity profile and time-average stream traces show that the wake and the separation process are asymmetric at orientations of 22.5 and 30°. The corresponding power spectra show additional peaks related to secondary vortical structures that arise from nonlinear interaction between the Karman vortices. The flow visualization images show the streamwise separation distance between the alternating vortices to be a function of cylinder orientation. Further, the flow approaches three dimensionality early, i.e., closer to the cylinder surface for the 22.5° orientation. The drag coefficient decreases with an increase in aspect ratio, while the Strouhal number is seen to increase with aspect ratio. The turbulence intensity is higher for the large aspect ratio cylinder and the maximum turbulence intensity appears at an earlier streamwise location. The overall dependence of drag coefficient and Strouhal number on orientation is preserved for the two aspect ratios studied.

DOI: 10.1061/(ASCE)0733-9399(2008)134:9(788)

CE Database subject headings: Cylinders; Drag; Coefficients; Experimentation.

Introduction

The study of bluff body wakes is important for applications in aerodynamics, wind engineering, and electronics cooling. Bluff body cross sections that are often employed are circular and rectangular (especially, square). The flow details behind these geometries depend on Reynolds number, blockage ratio, and free stream turbulence. For square/rectangular cross section geometries, the orientation with respect to the mean flow is another important parameter. At low Reynolds number, aspect ratio and end conditions play a significant role in determining the flow properties. Flow past a square cylinder resembles flow past a circular cylinder as far as instabilities are concerned. But the separation mechanism and the consequent dependence of lift, drag, and Strouhal number on the Reynolds number are significantly different. The separation points are fixed for the square cylinder either at the leading edge or the trailing edge, depending on the Reynolds number. The vortex formation region is significantly broader and longer for a square cylinder compared to the circular. The study on the effect of aspect ratio in the literature has been limited to a circular cylinder. The present study reports on experimental measurements of flow patterns in the wake of square cylinder cross section. Its sensitivity to aspect ratio and orientation with respect to the mean flow (namely, the incidence angle) are examined. Relevant studies from the literature are reviewed below.

Obasaju (1983) used hotwire anemometry to study the effect of cylinder orientation (0, 10, 13.5, 20, and 45°) at high Reynolds number. A reduction in drag coefficient and a sharp rise in Strouhal number was seen at an angle close to 13.5°. This effect was attributed to the shear layer reattachment over one of the edges of the cylinder. Knisely (1990) experimentally investigated the variation of Strouhal number of rectangular cylinders with side ratios in the range of 0.04–1 and angles of incidence from 0 to 90°. A sharp rise in Strouhal number for a small angle of incidence was reported.

Lee and Budwig (1991) studied the effect of aspect ratio for a circular cylinder at low Reynolds number using flow visualization and hotwire anemometry. For an aspect ratio greater than 60, a discontinuity in the Strouhal number value in the Reynolds number range ($64<R<130$) was reported. There is a stabilization effect on the wake for a small aspect ratio cylinder. The wake width increases with a reduction in aspect ratio. Stäger and Eckelmann (1991) studied the effect of end plates on the shedding frequency of circular cylinders in the intermediate range of Reynolds numbers (300–5,000). Near the end plate, the shedding frequency is lower than that at midspan. The end effect faded away with the increase in Reynolds number. König et al. (1993) studied the Strouhal number–Reynolds number relationship at various as-

[1]Lecturer, Dept. of Mechanical Engineering, National Institute of Technology Silchar, Silchar 788010 India. E-mail: sushant@nits.ac.in

[2]Professor, Dept. of Mechanical Engineering, Indian Institute of Technology Kanpur, Kanpur 208016 India (corresponding author). E-mail: panig@iitk.ac.in

[3]Professor, Dept. of Mechanical Engineering, Indian Institute of Technology Kanpur, Kanpur 208016 India. E-mail: kmurli@iitk.ac.in

Note. Associate Editor: Brett F. Sanders. Discussion open until February 1, 2009. Separate discussions must be submitted for individual papers. The manuscript for this paper was submitted for review and possible publication on May 22, 2007; approved on February 1, 2008. This paper is part of the ***Journal of Engineering Mechanics***, Vol. 134, No. 9, September 1, 2008. ©ASCE, ISSN 0733-9399/2008/9-788–803/$25.00.

pect ratios and end conditions. The discontinuity in the relationship was attributed to the oblique shedding angle and transition in discrete shedding modes.

Szepessy and Bearman (1992) studied the effect of aspect ratio (0.25–12) and end plates for flow past a circular cylinder at high Reynolds number ($8\times10^3<R<1.4\times10^5$). With appropriate end plates they showed that wake flow is two dimensional. Norberg (1993) reported the Strouhal numbers for rectangular cylinders of various side ratios (1–5) and incidence angles (0–90°) for Reynolds numbers in the range $400-3\times10^4$ from hotwire anemometry measurements. For intermediate angles, Strouhal number and drag coefficient were found to be nearly constant when based on the projected dimension of the cylinder. Norberg (1994) studied the effect of aspect ratio for flow past a circular cylinder over a wide range of Reynolds numbers starting from laminar to transition and ultimately turbulent flow. The critical Reynolds number for the onset of vortex shedding was found to be constant for aspect ratios (ARs) larger than 40 and was delayed for lower aspect ratios. At an aspect ratio larger than 100 the Strouhal number was found to be independent of aspect ratio.

Mansy et al. (1994) reported laser Doppler velocimeter (LDV) data based on an investigation of flow past a circular cylinder over a range of Reynolds numbers. The writers observed the three-dimensional structures to be strongest close to the cylinder during formation of primary vortices. The larger scales are amplified and the smaller scales attenuated in the downstream direction. Brede et al. (1996) did a particle image velocimetry (PIV) study for flow past a circular cylinder at Reynolds numbers between 160 and 500. Two modes of secondary vortices (A and B) with different wavelengths were observed. They showed the effect of aspect ratio on the spanwise wavelength and circulation of streamwise eddies. Williamson (1997) reviewed the nature of flow past a circular cylinder at low Reynolds numbers. The flow three dimensionality in nominally two dimensional geometry at low Reynolds numbers was attributed to the vortex dislocation. One other phenomenon responsible for three dimensionality was shown to be the oblique shedding.

Dutta et al. (2003) reported on the sensitivity of the wake behind a square cylinder to the angle of incidence ($\theta=0-60°$) and high Reynolds numbers (1,340, 4,990, and 9,980) based on hot-wire anemometry measurements and smoke visualization. They observed reduced drag coefficient and higher Strouhal number with an increase in the orientation angle. Oudheusden et al. (2005) studied the vortex shedding characteristics in the near wake of a square cylinder at incidence to the mean flow for Reynolds numbers of 4,000, 10,000, and 20,000 using PIV. The writers used proper orthogonal decomposition (POD) to reconstruct the phase-averaged flow field from time uncorrelated data. The pattern of individual POD modes was found to be a function of the incidence angle. For a cylinder at incidence a striking difference in vortex formation from the upper and lower side of the body was evident from various phase angles.

The literature review indicates the importance of cylinder orientation for bluff bodies at low Reynolds numbers. There is an additional influence of aspect ratio that contributes to three dimensionality, but has been experimentally investigated only for circular cylinders. For a square cylinder, a joint study of cylinder orientation and aspect ratio is not available. The present work reports measurements in the wake of a square cylinder at an intermediate Reynolds number of 410. Four cylinder orientations (0–45°) and two aspect ratios, namely 16 and 28, are considered. The blockage ratio was less than 7% and is not an influential parameter in the study. The velocity field is mapped using PIV and hotwire anemometry (HWA). Flow visualization images compare the flow structures that appear in the wake. The sensitivity of the flow properties to cylinder orientation and aspect ratio are reported.

Apparatus and Instrumentation

Experiments have been carried out in a vertical test cell made of Plexiglas with air as the working fluid (Fig. 1). The test cell has two optical windows, one for the passage of the laser sheet and the other for recording by the camera. The cross section of the test cell is 9.5×4.8 cm^2 and the overall length is 2 m. The active length of the test cell where measurements have been carried out is 0.3 m. A contraction ratio of 10:1 ahead of the test section has been used. Cylinders of square cross section (3 and 3.4 mm edge) used for experiments are made of Plexiglas and machined for sharp edges. Therefore, the aspect ratio in our experiment is equal to 16 (48/3) and 28 (95/3.4). Limited data at an aspect ratio of 60 have been obtained in a separate wind tunnel (cross section 300 $\times$160 mm) using a square cylinder of 5 mm. The cylinder is mounted horizontally with its axis perpendicular to the flow direction. It is supported along the two side walls. With reference to Fig. 1, the x axis is vertical and aligned with the mean flow direction. The z axis coincides with the cylinder axis and the y axis is perpendicular to x and z. The distance of the cylinder axis from the outlet of the contraction is at least ten times the cylinder edge to ensure adequate decay of free stream disturbances (Sohankar et al. 1998).

End plates have been used in the past experiments to minimize the wall boundary layer effect, suppress three dimensionality, and for parallel vortex shedding. Measurements were carried out with and without end plates for the square cylinder over a Reynolds number range of 200–600. The endplate parameters were based on that of Norberg (1994) and Stansby (1974). For configurations with and without end plates, the difference in the velocity profile at different spanwise z locations was found to be minimal. Hence, the effect of endplates on the velocity profile was insignificant in both spanwise and streamwise direction. The Strouhal number was also measured under these conditions. The difference in Strouhal number with and without endplates was less than $\pm2\%$. The low turbulence level in the test section of the present study and the proximity of the cylinder to the inlet of the test section are responsible for the thin boundary layer and hence a small endwall effect. The data reported in the present study do not utilize end plates.

The flow in the test section is set up by a suction pump driven by a single phase motor at the outlet. The power supply to the pump was stabilized to provide a practically constant input voltage to the motor. The free stream turbulence level in the approach flow was quite small; it was found to be less than the background noise of the anemometer ($<0.05\%$). Flow parallelism in the approach flow was better than 98% over 95% of the width of the test cell. Stable velocities in the range of 0.5–3 m/s were realized in the test cell to cover the Reynolds number range of 100–800.

Measurements of the velocity field over selected planes were carried out using a PIV system. It comprises a double pulsed Nd:YAG laser (*new wave lasers*, $\lambda=532$ nm), 15 mJ/pulse, a Peltier-cooled 12 bit charge-coupled device (CCD) camera (*PCO Sensicam*) with a frame speed of 8 Hz, a synchronizer, frame grabber, and a dual processor PC. The CCD consists of an array of $1{,}280\times1{,}024$ pixels. A Nikon 50 mm manual lens with $f^{\#}=1.4$ was attached to the CCD camera for covering the field of

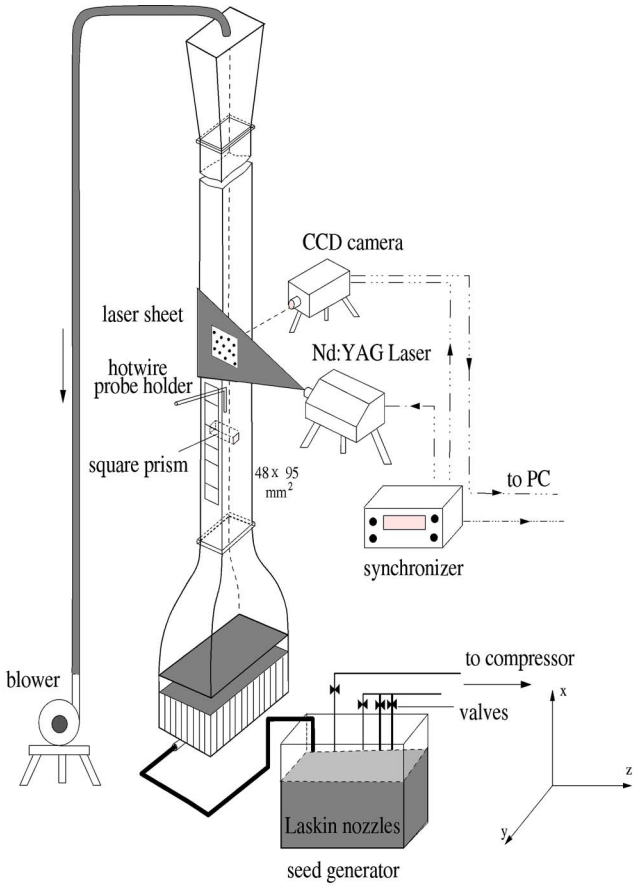

(a)

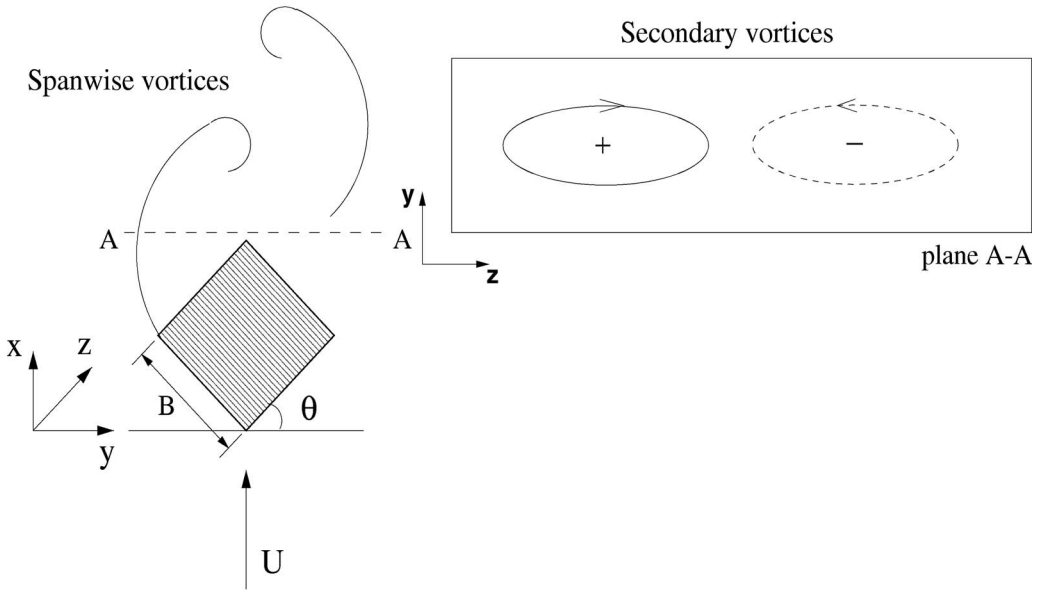

(b)

Fig. 1. (a) Schematic drawing of experimental setup; (b) schematic drawing of prismatic cylinder and associated vortices

Table 1. Comparison of Drag Coefficient with Literature for Flow Past Square Cylinder

Writers	Nature of study	Aspect ratio	Blockage	R	$\bar{C}_D$
Davis et al. (1984)	Numerical (2D)/experimental	1	0.167	470	1.95
Sohankar et al. (1999)	Numerical (3D)	6	0.055	400	1.67
Saha et al. (2003)	Numerical (3D)	6–10	0.100	400	2.10
Li and Humphrey (1995)	Numerical (2D)	6.44	0.192	500	1.98
Present	Experimental	16	0.030	410	2.29 (2.60)
		28	0.070	420	2.03 (2.57)

Note: Values within parenthesis include the contribution of velocity fluctuations on the time averaged drag.

interest. The field of view for PIV measurements was 40 mm by 35 mm. Velocity vectors were calculated from particle traces by the adaptive cross-correlation method (Panigrahi et al. 2005). The final interrogation size was 16×16 pixels from an initial starting value of 64×64 and 5,561 velocity vectors were obtained with a spatial resolution of 0.5 mm. Inconsistent velocity vectors were eliminated by local median filtering. The laser pulse width was 20 μs and the time delay between two successive pulses was varied from 40 to 200 μs depending on the fluid velocity (Keane and Adrian 1990). The time-averaged velocity field was obtained by averaging a sequence of 200 velocity vector images, corresponding to a total time duration of 50 s. Proper seeding is essential for good PIV images, particularly when recirculation regions are to be imaged. In the present work, seed particles were added to the main flow by a number of copper tubes upstream of the honeycomb section. Multiple holes were drilled in these copper tubes to make the seeding uniform over the entire test cross section. Laskin nozzles were used to produce seeding particles from corn oil. The mean diameter of the oil particles was estimated to be 2 μm. The instantaneous flow visualization images were recorded using the PIV system itself with a reduced particle density with a laser pulse width of 25 μs and an exposure time of 4 ms.

Local time-averaged velocity and velocity fluctuations were measured using a hotwire anemometer (DANTEC). An X-wire probe was used for measuring two components of velocity. With the square cylinder placed horizontally, the X configuration was formed in the vertical plane. The two wires of the probe were calibrated against a pitot-static tube connected to a digital manometer (FURNESS CONTROLS, 19.99 mm H_2O). The anemometer output voltage was collected in a PC through a data acquisition card (*National Instruments*) with LabVIEW software. The measurement procedure adopted in the present work is similar to that presented by the writers elsewhere (Dutta et al. 2003, 2007). In the low velocity regime, measurements with the pitot-static tube as well as the hotwire anemometer are prone to errors. These can arise from higher order physical phenomena including free convection and probe interference effects. The errors can be controlled by using a pitot-static tube of small diameter (3 mm in the present study); in addition the hotwire probe in the present work was operated at a lower temperature (of around 150°C) leading to minimization of free convection and radiation errors, without loss of sensitivity. The power spectra of the velocity fluctuations were determined using the fast Fourier transform (FFT) algorithm. The sampling frequency used was 1,000 Hz, the signal length being 20 s. A band pass filter in the range of 0.1 Hz–1 kHz was additionally used.

Flow visualization was carried out in the test cell using a light sheet of a pulsed Nd:YAG laser. The images were recorded with a CCD camera synchronized with the firing of the laser. The light sheet and the camera were perpendicular to each other. The particle density was adjusted by lowering the Laskin nozzle pressure to obtain a higher sensitivity of the images of the flow structure.

Uncertainty and Repeatability

The seeding of flow with oil particles, calibration, laser light reflection, background illumination, image digitization, cross correlation calculation, velocity gradients, and out-of-plane particle motion affect the accuracy of PIV measurements. Tracer particles need to follow the main air flow without any lag. For the particle size utilized and the range of frequencies in the wake, an expected slip velocity error of 0.3–0.5% relative to the instantaneous local velocity is expected. A second source of error in velocity measurement is due to the weight of the particle. In the present experiments, the weight effect on the seed particles was examined by conducting experiments at a fixed Reynolds number by varying the size of the cylinder. The streamline plot and the dimensionless size of the recirculation region were found to be identical in each case, and independent of the fluid velocity. The noise due to background light was minimized by using a band-pass filter (at the wavelength of the laser) before the camera sensor. The x and y component velocity profiles from PIV measurements compared very well with those from the hotwire in the far field region, confirming the proper implementation of both the techniques and the measurement procedure. From repeated measurements at the zero degree cylinder orientation (with Reynolds number kept constant to within ±1%), the uncertainty in drag coefficient was determined to be within ±5%. The uncertainty in Strouhal number was ±2%.

Validation of Experimental Data

Measurements have been compared against published results in terms of drag coefficient, Strouhal number, and vorticity patterns. Table 1 presents a comparison of time-averaged drag coefficient of a square cylinder for zero angle of incidence. For three-dimensional numerical simulation, the drag coefficient is a value averaged over the entire span of the cylinder. The experimental value is that of the midplane, obtained by a wake survey method. The drag coefficient from all studies are in the range of 1.95–2.6. Fig. 2 compares the Strouhal number from the present work with that of other investigations at similar Reynolds number and a zero degree orientation. There is a satisfactory match between our data (AR=28) and that of Okajima (1982) at lower Reynolds number ($R < 300$). At higher Reynolds number, there is a reasonable match between the present data and that of Norberg (1994). The comparison of Strouhal number data with other investigations (Davis et al. 1984; Sohankar et al. 1999; Sohankar et al. 2003) show intrinsic uncertainty in measurements at intermediate Rey-

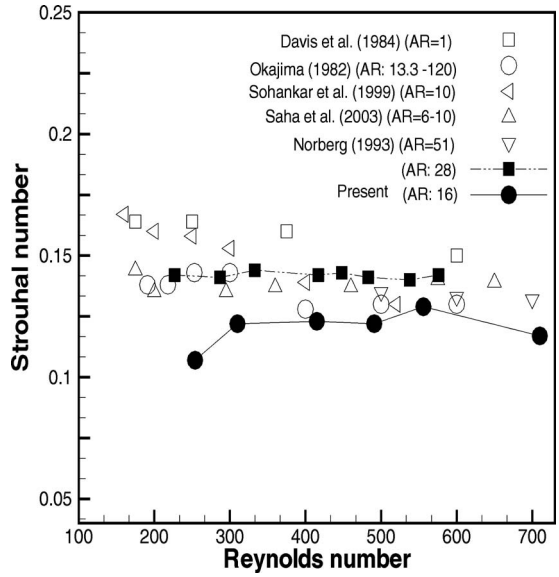

Fig. 2. Strouhal number versus Reynolds number value comparison with literature

nolds numbers. Against this background, the match shown in Fig. 2 can be taken to be satisfactory.

Fig. 3 shows the instantaneous streamwise vorticity contours (ω_x) above a circular cylinder obtained in the present work using PIV. The axis of the vorticity component is along the flow direction. The Reynolds number of the present work is 330. At this Reynolds number, secondary (streamwise) vortices are generated along with the spanwise (Karman) vortices. The secondary vortices are arranged along a line parallel to the cylinder axis. The sense of rotation changes along the spanwise direction. The spanwise wavelength of the secondary vortices is around one cylinder diameter, the spacing between the vorticity peaks being, in general, a constant. This compares well with the PIV results of Brede et al. (1996). The results of Brede et al. (1996) are at Reynolds number 290. Overall, the favorable comparison of vorticity patterns, Strouhal number, and drag coefficient value with the literature confirms the correct implementation of the experimental procedure in the present study.

Results and Discussion

Results have been presented for a square cylinder oriented at various angles to the incoming flow. The ranges of parameters considered in the study are as follows: incidence angle 0–45°; Reynolds number 410; and aspect ratio 16 and 28. Mirror images

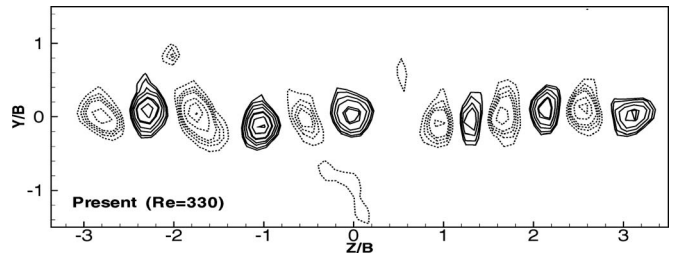

Fig. 3. Instantaneous vorticity contours on y-z plane above circular cylinder

of the 0–45° flow fields are produced for cylinder angles between 45 and 90°. The drag coefficient and Strouhal number are based on B, the cylinder dimension irrespective of the cylinder angle. It is expected that an increase in the projected dimension due to the cylinder orientation will increase the drag coefficient and reduce the Strouhal number. Experiments show that drag coefficient decreases, attains a minimum, and then increases with an increase in the orientation angle. The Strouhal number shows an opposite trend. The reasons for this behavior have been explored in the study.

The change in the angle of the cylinder affects the wake primarily due to the following two factors: (1) change in the projected dimension normal to the flow; and (2) movement of the point of separation and hence the position of the dividing streamline. The dividing streamlines are symmetric for 0 and 45°, but evolve unsymmetrically at all other angles. The loss of symmetry is felt in the time-averaged velocity distribution. The projected dimension affects the minimum streamwise velocity in the near wake. The lowest u velocity is to be expected for an angle of 45°, in comparison to all other angles. For a square cylinder, the points of separation are fixed at the upstream corners. There is a possibility of flow detaching from the upstream corner, closing in on the cylinder, and separating once again from the rear corners. When the square cylinder is inclined to the mean flow, only one pair of corners contribute to flow separation. Change in aspect ratio influences the degree of three dimensionality of the flow field. A vigorous third component of velocity along the cylinder axis is indicative of a weakened wake in the main flow direction.

The thrust of the present experimental study is to examine the sensitivity of the wake of the cylinder with respect to orientation and aspect ratio. Accordingly, the results of the present study have been discussed in the following sequence: (1) drag coefficient and Strouhal number; (2) flow visualization; (3) time-averaged stream traces; (4) time-averaged velocity profiles; (5) recovery of centerline velocity; (6) time-averaged velocity fluctuation; (7) time-averaged vorticity; and (8) power spectra.

Strouhal Number and Drag Coefficient

The Strouhal number has been calculated from the location of the spectral peak of the velocity trace as recorded by the hotwire anemometer. The time-averaged drag coefficient has been calculated using the wake survey method based on applying a momentum balance approach over a control volume around a cylinder. Drag coefficient reported here arises from the combined effect of momentum deficit and time-averaged turbulent stresses at the outflow plane of the wake. It has been determined as a time-averaged quantity from a PIV data set of 200 images. The drag coefficient has been determined from the profiles of velocity and velocity fluctuations across the entire test cell at a streamwise location of $x=10$. Farther downstream ($x=15$), the time-averaged velocity field was significantly distorted by the presence of the wall and was not preferred. Since the plane $x=10$ is not sufficiently far away from the cylinder, the correction arising from turbulent stresses is expected to be significant. The drag coefficient has been calculated from the extended formula

$$C_D = 2\int_{-\infty}^{+\infty} \frac{u}{U}\left(1-\frac{u}{U}\right)dy + 2\int_{-\infty}^{+\infty}\left(\frac{\overline{v'^2}-\overline{u'^2}}{U^2}\right)dy \qquad (1)$$

The first term is the momentum deficit of the time-averaged flow field and the second term is the contribution of the turbulent fluc-

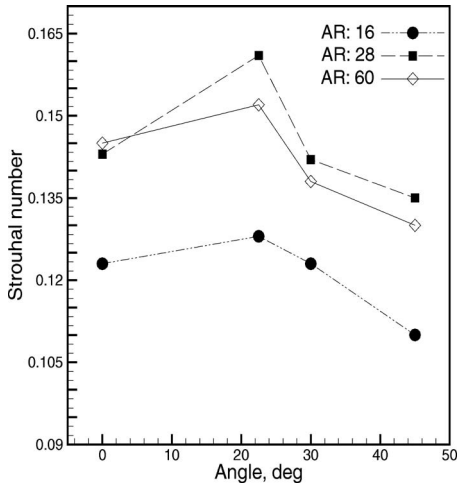

Fig. 4. Variation of Strouhal number with cylinder orientations for three aspect ratios at R=410

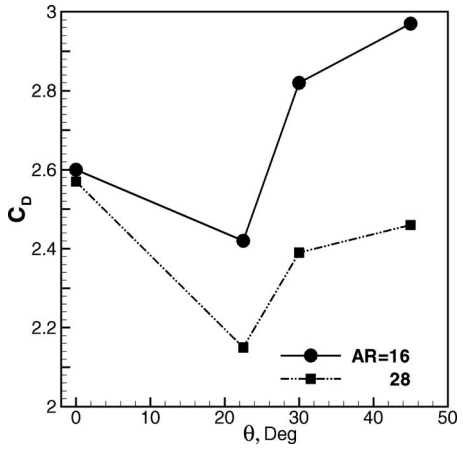

Fig. 5. Variation of time-averaged drag coefficient with cylinder orientation for two aspect ratios at R=410

tuations. In all experiments, the second term was found to be 10–15% of the total drag.

Fig. 4 shows the Strouhal number variation with cylinder orientation at R=410. The trend with respect to the incidence angle is similar for all aspect ratios with a maximum Strouhal number at the 22.5° orientation. The Strouhal number increases from the 0° incidence angle to 22.5°, with a subsequent drop for an increase in the incidence angle. From experiments, Chen and Liu (1999) observed an increase in the Strouhal number with respect to the incidence angle for a square cylinder until 17° (at which S was 0.187) followed by a marginal drop to an asymptotic value of about 0.175. The Reynolds number range considered was 2,000–21,000. The incidence angle that produces a maximum in Strouhal number was attributed to the onset of flow reattachment to the side face of the cylinder. The overall trend in the Strouhal number variation with respect to the orientation is quite similar for the two studies. The difference in the magnitudes of the Strouhal number between the present study and those of Chen and Liu (1999) can be attributed to the difference in Reynolds number.

The Strouhal number variation with incidence angle is related to an increase in the projected dimension of the cylinder with respect to the incoming flow. The vortex shedding frequency is influenced by the width between two free shear layers and the free stream velocity. The increase in the incidence angle leads to an increase in the distance between the two free shear layers. Therefore, an increase in the incidence angle results in a reduced interaction between the two shear layers and a drop in the Strouhal number. This explanation is applicable for angles beyond 22.5°. It is also possible that the separating shear layer on one side draws the neighboring vortex in the opposite shear layer towards it, leading to an increase in the Strouhal number. Thus, a maximum seen at 22.5° incidence angle is due to competing effects of an increased projected dimension and a shorter vortex roll-up distance. These aspects are examined further in the following sections.

The Strouhal number increases with aspect ratio for all angles (Fig. 4). The Strouhal number increases from 0.124 to 0.145 with an increase in aspect ratio from 16 to 28 at 0° orientation. There is, however, only a small difference in the Strouhal number between AR=28 and 60. Norberg (1994) observed a jump in the Strouhal number from about 0.14 to 0.16 for a circular cylinder at an aspect ratio equal to 30. Lee and Budwig (1991) observed a similar behavior of the Strouhal number with respect to aspect ratio for a circular cylinder with a maximum in the Strouhal number attained at about AR=35. For a subsequent increase in aspect ratio, no change in the Strouhal number value was observed. The difference in magnitudes of Strouhal number and the critical aspect ratio among these studies can be attributed to the differences in the Reynolds number and the geometry of the bluff body. Overall, it can be concluded that the effect of aspect ratio on the Strouhal number is similar for circular and square cylinders.

The total drag coefficient can be obtained from the complete velocity profile measurements in all spanwise planes due to the three dimensionality of the flow field. The full-cylinder drag coefficient will be lower than that of the midplane. From the velocity measurements in the spanwise direction, it was observed that the drag coefficient diminishes uniformly towards the side walls. Thus the trends seen in the midplane carry over to the entire cylinder.

Fig. 5 shows the effect of cylinder orientation on the time-averaged drag coefficient for two aspect ratios. A minimum in drag coefficient is observed at 22.5° for both aspect ratios. The magnitude of drag coefficient is higher at the lower aspect ratio (AR=16) compared to the higher (AR=28). This trend is opposite to that of the Strouhal number (Fig. 4), where the Strouhal number at the higher aspect ratio is also higher. A higher Strouhal number is an indication of the positive interaction between the opposed shear layers that feed the fluid to the growing vortex and cause early shedding. It also leads to weakening of the wake by increased mixing and therefore a reduction in the drag coefficient.

The influence of aspect ratio on the Strouhal number and drag coefficient can be explained in terms of the strength of flow along the length of the cylinder. The secondary flow can be seen as a mechanism by which the overall pressure difference across the cylinder (and hence C_D) is reduced. Fig. 5 shows that a minimum in drag coefficient occurs at 22.5°; the corresponding strength of the secondary flow would be a maximum. The particle traces support this expectation. Since interaction of shear layers is predominantly a two-dimensional phenomenon, secondary flow does not alter Strouhal number and an asymptotic limit is reached for increasing aspect ratios.

The trends seen in Figs. 4 and 5 are explained in terms of the detailed flow fields in the following sections.

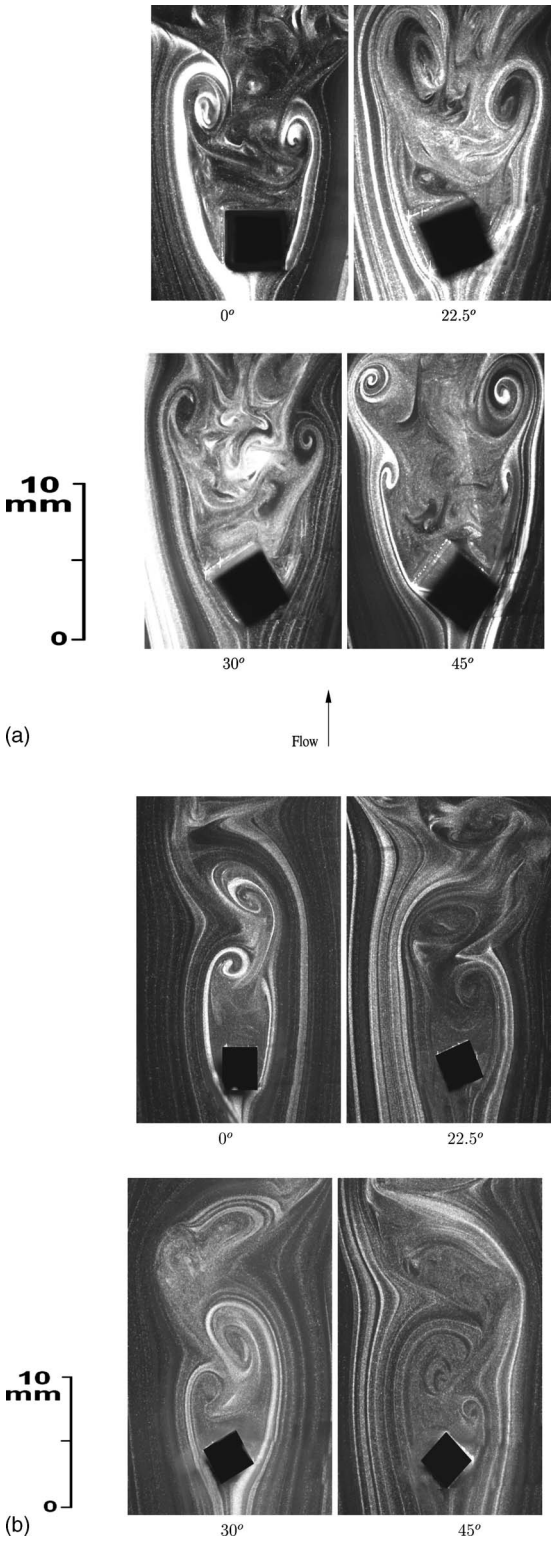

Fig. 6. Near wake instantaneous particle traces behind square cylinder for different orientations at R=410: (a) AR=16; (b) AR=28; 10 mm scale is included with images

Flow Visualization

Particle traces for different cylinder orientations (0, 22.5, 30, and 45°) are shown in Fig. 6. The interest here is in examining the possibility of shear layer reattachment over the cylinder surface and the distance over which the shear layer rolls up. To examine these effects, the camera was held at a small inclination ($\simeq 3°$) with respect to the cylinder axis. The images shown are instantaneous. For angles of 0 and 45°, flow separation is from the upstream corners of the cylinder. The separated shear layers diverge in the streamwise direction and the possibility of shear layer reattachment is absent for both aspect ratios. At other angles (22.5 and 30°), flow separation is asymmetric with the shear layer from one side diverging away from the cylinder midplane. At the other side, the shear layer leaving a corner remains close to the cylinder surface that acts as an after-body. There are two asymmetric recirculation zones behind the two downstream edges of the cylinder. The shear layers do not allow an abrupt change in the slope of the streak lines. It is hence to be concluded that experiments do not show reattachment followed by a second separation. The distance over which the shear layers roll up is a measure of the time taken for instability to set in, and hence inversely to Strouhal number. For 0 and 45°, the shear layers on each side of the cylinder roll up over similar distances, and a well-defined Strouhal number is obtained. At other orientations, the shear layers on each side are markedly different, and two vortex shedding frequencies are realized. It is also possible that the vortex shedding frequency corresponding to the vortex that rolls up over a shorter distance drives the unsteadiness in the wake. In this context, a single Strouhal number is once again realized. At other angles, the Strouhal number is determined by the vortex that rolls up over a shorter distance (though modulated by the second longer shear layer). This point has been clarified from the power spectra discussed in the "Power Spectra" section.

The flow visualization images of Fig. 6 also explain the reduction in drag coefficient at certain angles. The drag coefficient is expected to increase continuously with angle due to increased blockage of flow. Simultaneously, the relatively longer shear layer formed at angles other than 0 and 45° results in asymmetry of the wake, larger transverse velocities, better mixing, and hence a higher base pressure. The distance between the vortices in the opposite shear layer in the flow visualization images (Fig. 6) confirm this expectation. Thus, at an intermediate angle (22.5° in the present study), a minimum in drag coefficient is realized. The effect of aspect ratio on the Strouhal number and drag coefficient (Figs. 4 and 5) is also explained from the flow visualization pictures of Fig. 6. The separation between the vortices of opposite shear layers is lower for AR=28 compared to AR=16 (Fig. 6). Thus the interaction between alternating vortices is lower for the small aspect ratio cylinder leading to reduction in Strouhal number and increase in drag coefficient.

Fig. 7 shows the flow visualization pictures in the x-z plane at different cylinder orientations for aspect ratios of 16 and 28. The objective is to show the spanwise variation and hence the three dimensionality of flow behind the square cylinder. Mushroom type vortical pair structures are seen in the visualization images. These structures are similar to the Mode B type seen behind a cylinder wake (Williamson 1996). However, these structures are comparatively more irregular in the spanwise plane for the present study possibly due to higher Reynolds number and vortex dislocation. The three dimensionality appears early for the low aspect ratio cylinder compared to that of the large aspect ratio. For AR=28, the three-dimensional vortex structures appear at streamwise x locations that depend on the cylinder orientation. The three dimensionality shows up very close to the cylinder for an orientation equal to 22.5° (AR=28). The early appearance of three dimensionality (3D) may also be correlated to the minimum drag at this orientation. The x location at which three dimensionality appears is also related to the evolution of streamwise turbu-

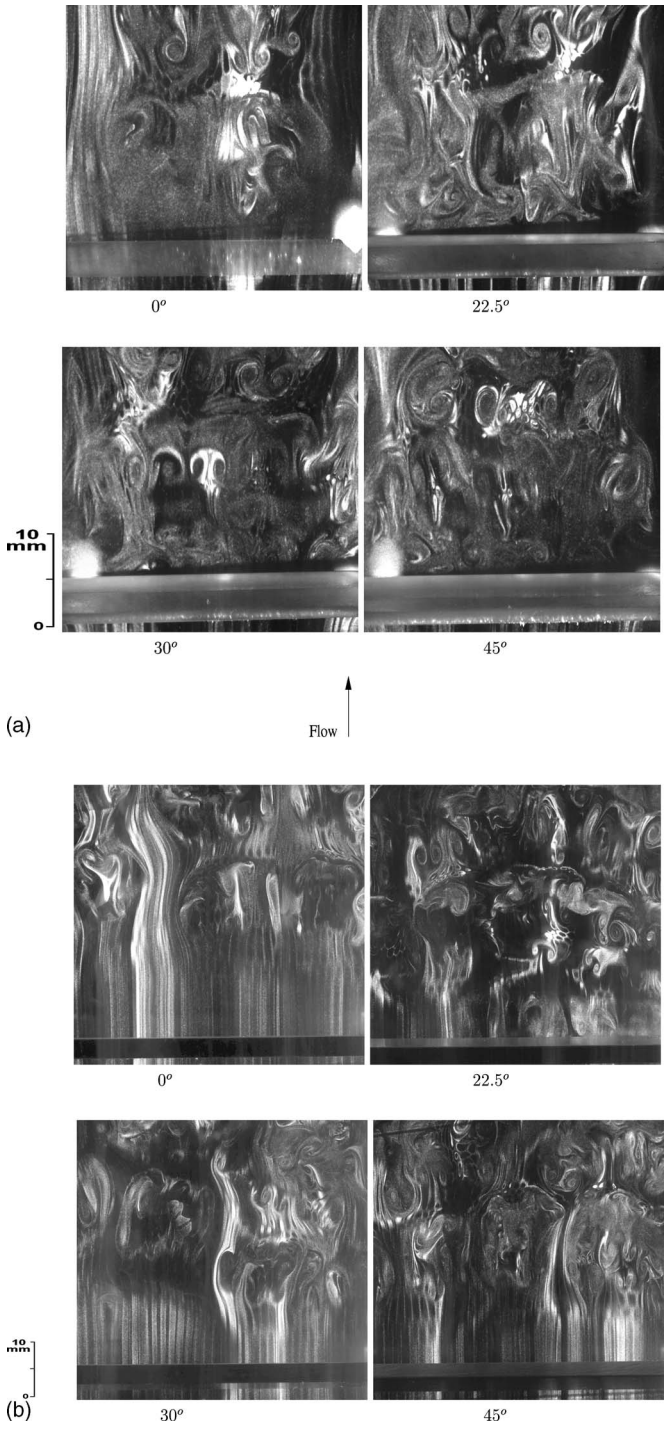

Fig. 7. Spanwise near-field particle traces in $x-z$ plane at $y=0.5$ behind square cylinder at different cylinder orientations at $R=410$: (a) AR=16; (b) AR=28; 10 mm scale is included with images

lent intensity. As discussed in a later section, turbulence intensity was observed to peak earlier at a cylinder angle of 22.5°. There is no spanwise variation in the onset of 3D flow structures for any of the cylinder orientations. This indicates parallel vortex shedding behind the square cylinder. At low aspect ratio (AR=16), the three dimensionality appears closer to the cylinder; in addition this location is insensitive to the cylinder orientation.

Time-Averaged Stream Traces

Fig. 8 compares the time-averaged stream traces in the wake of the cylinder at Reynolds numbers of 410 for two aspect ratios (16 and 28). The stream traces are plotted at the midplane ($z=0$) of the cylinder. Two bubbles with opposed direction of circulation form behind the cylinder. At all cylinder orientations, the size of the recirculation bubble in the streamwise as well as the transverse direction is greater for the low aspect ratio cylinder compared to the high. The larger recirculation bubble for low aspect ratio indicates a greater formation length of the vortex. The increase in formation length at the lower aspect ratio can be related to the early appearance of spanwise variation, namely three dimensionality of the flow field. It correlates with the higher drag coefficient shown in Fig. 5. Similarly, the wake width is comparatively smaller for the high aspect ratio cylinder. The smaller recirculation bubble size and wake width for the high aspect ratio cylinder relates to the corresponding lower drag coefficient of Fig. 5.

The recirculation bubbles of Fig. 8 also demonstrate that flow is asymmetric when the orientation of the cylinder is 22.5 or 30°. The separating streamlines on each side of the recirculation bubble are oriented at an angle with respect to the mean flow, indicating greater interaction between the two. The core location and transverse extent of the recirculation bubbles are different for these cylinder orientations. The effect is clearly evident for the higher aspect ratio.

Of the two aspect ratios tested, the size of the recirculation region and the drag coefficient were higher for the lower aspect ratio. Thus, the effect of lowering aspect ratio is to stabilize the shear layers, enlarge the wake, and lead to higher drag on the cylinder. The stabilization effect in-turn, lowers the Strouhal number. The intensifying of the flow in the third dimension at the lower aspect ratio has only a secondary influence on the average flow properties.

Time-Averaged Velocity Profiles

Profiles of two components of the time-averaged velocity are compared in Fig. 9 for the four incidence angles (0, 22.5, 30, and 45°). The comparison is presented for four downstream locations ($x=2$, 4, 6, and 8). These streamwise locations have been selected to include important regions of interest, namely the prerecirculation bubble ($x=2$), the core recirculation bubble ($x=4,6$), and postrecirculation region ($x=8$). Velocity has been nondimensionalized with that of the incoming stream and x-y coordinates are nondimensionalized with the cylinder edge. With an increase in the downstream distance, the x component of the centerline velocity recovers towards the free-stream value, while the y-component velocity approaches zero. The wake becomes broader due to entrainment of the fluid into the wake. In near wake, the wake size increases rapidly because of displacement by the two oppositely oriented eddies. In the far downstream, the wake size reaches a limiting value since the eddies are weakened by viscous dissipation and diffusion.

Fig. 9 shows that the u- and v-velocity profiles have a strong dependence on aspect ratio. For the streamwise velocity, recovery is much faster for the higher aspect ratio cylinder when compared to the lower. When the aspect ratio is high, the initial recovery of streamwise velocity is faster when compared to the low aspect ratio. This is related to the size of the recirculation bubble in the streamwise direction and its location with respect to the x-z midplane. The u-velocity profile at 22.5° orientation shows minimal

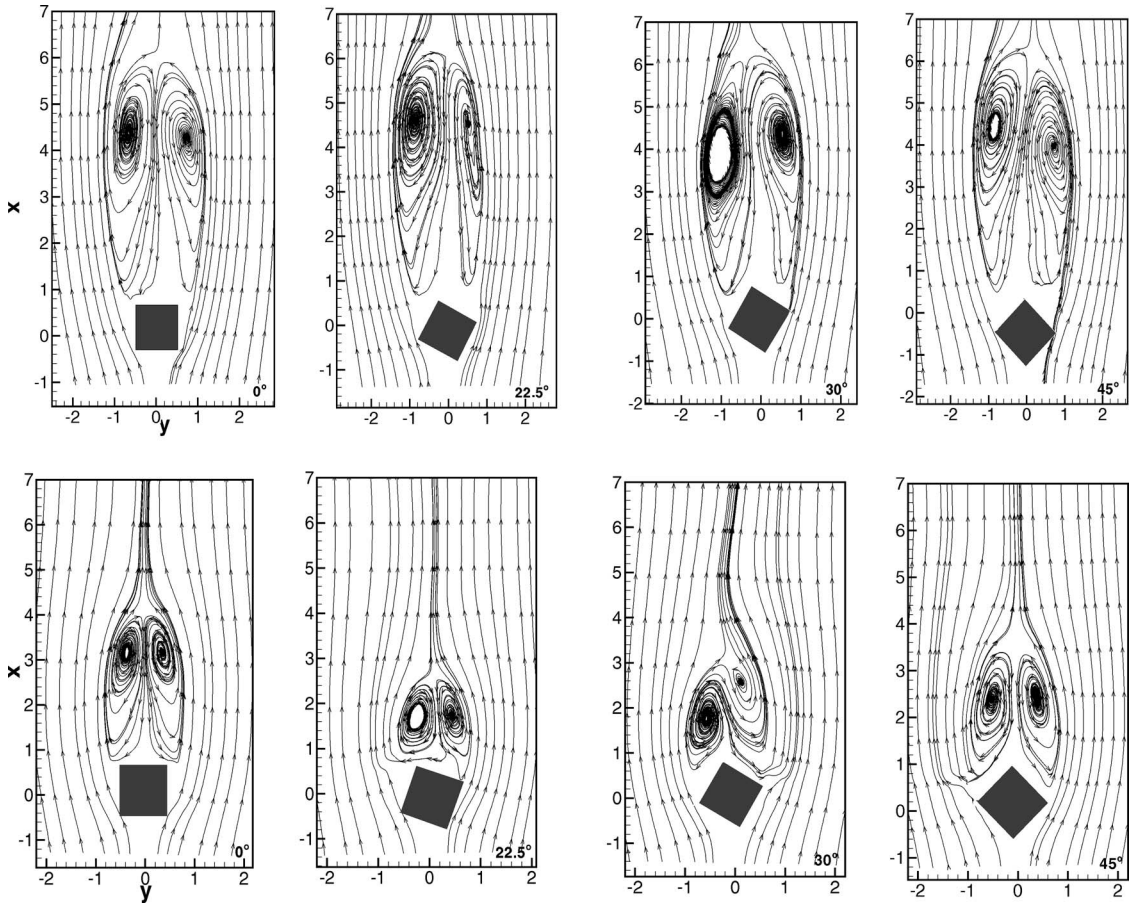

Fig. 8. Time-averaged stream traces in wake of square cylinder at R=410; influence of cylinder orientation; first row, AR=16; second row AR=28

velocity deficit compared to other cylinder angles for both aspect ratios. This trend is in conformity with the lowest drag coefficient seen at this orientation (Fig. 5). The streamwise velocity profile for the low aspect ratio cylinder continues to develop until the location of $x=8$. In contrast, the streamwise velocity profile for high aspect ratio at 22.5 and 30° orientations attain a self-similar profile at $x=8$.

Both positive and negative transverse velocities are seen above and below the midplane of the cylinder. Thus, fluid particles are entrained from each side into the wake. Compared to streamwise velocity, the transverse v velocity shows greater variation with respect to the incidence angle and aspect ratio. At $x=2$, the v-velocity profile shows similar variation for all incidence angles at AR=16. This is because $x=2$ is a location upstream of the recirculation bubble for all cylinder orientations at this aspect ratio. In contrast, the v-velocity profile shows significant variation as a function of incidence angle for the high aspect cylinder (AR=28). This is because $x=2$ is a location upstream of the recirculation bubble at 0° and downstream of the recirculation bubble at 22.5° (Fig. 8). Therefore, on an average, the direction of v velocity at 22.5° is opposite that at 0°. Similarly, the v velocity at $x=6$ shows an opposite trend when compared to $x=2$ for AR =16. Immediately upstream of the core of the recirculation bubble, the v-velocity profile shows dual peaks at the $x=4$ location for all incidence angles and AR=16. Similar dual peaks are observed at $x=2$ and $\theta=45°$ for AR=28. This is due to the rapid change streamwise velocity near the core location. The v-velocity profile is asymmetric for 22.5 and 30° orientations. Therefore, the local instability modes and their amplification rate are altered for these orientations of the square cylinder leading to the appearance of additional harmonics in the flow fluctuations. These are shown in power spectra section in the form of power spectra. These modes are not as clearly evident at AR=16 due to an early influence of three dimensionality (Fig. 7). The asymmetric separation processes for 22.5 and 30° are clear from the v-velocity profile when compared to the u velocity. At the end of the recirculation bubble, the transverse velocity magnitudes reduce, leading to a slow but definite recovery of the streamwise velocity.

Recovery of Centerline Velocity

Centerline recovery of the streamwise velocity and decay of the transverse velocity for various angles are compared in Fig. 10. The transverse velocity has been plotted along the x axis at a particular offset location from the cylinder centerline ($y=1$). The u velocity is zero on the cylinder surface and is negative (in the time-averaged sense) up to a certain downstream distance. Later, it increases with the x coordinate and reaches an asymptotic value.

Two factors play a major role in determining centerline recovery of velocity. One is the wake size and the second is base pressure on the rear surface of the cylinder. With downstream distance, the wake becomes broader due to entrainment of the fluid and the average pressure difference between the wake and the outer flow diminishes. Hence, the pressure difference between the core of the wake and the external flow determines the initial

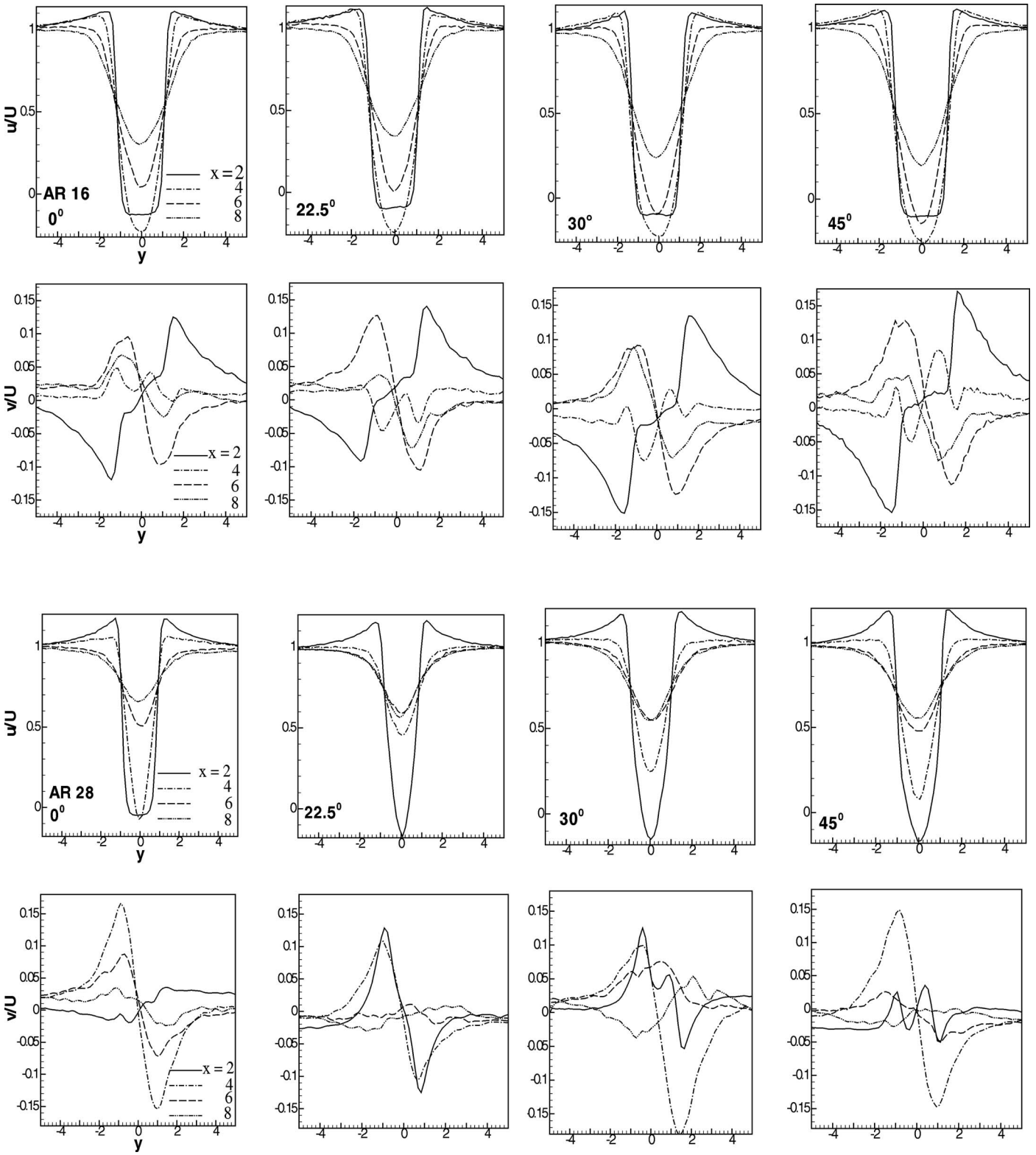

Fig. 9. Time-averaged u and v velocity profiles at four downstream locations (x=2, 4, 6, and 8) for two aspect ratios (16 and 28) and four cylinder orientations (0, 22.5, 30, and 45°) at R=410

recovery. Downstream recovery in velocity depends on flow readjustment in the form of the fluid drawn into the wake from the external flow. The first factor is a strong function of cylinder orientation. Hence the base region of the cylinder carries these characteristics; at longer distances downstream, these factors are less significant.

Fig. 10 shows that centerline recovery is faster for the high aspect ratio cylinder. For both aspect ratios, the centerline velocity reaches an asymptotic value in the range of 0.6–0.65. The decay of transverse velocity is also faster for the high aspect ratio cylinder. The asymptotic limit of u velocity is reached at around x=15 and 7, respectively, for the low and high aspect ratios. This

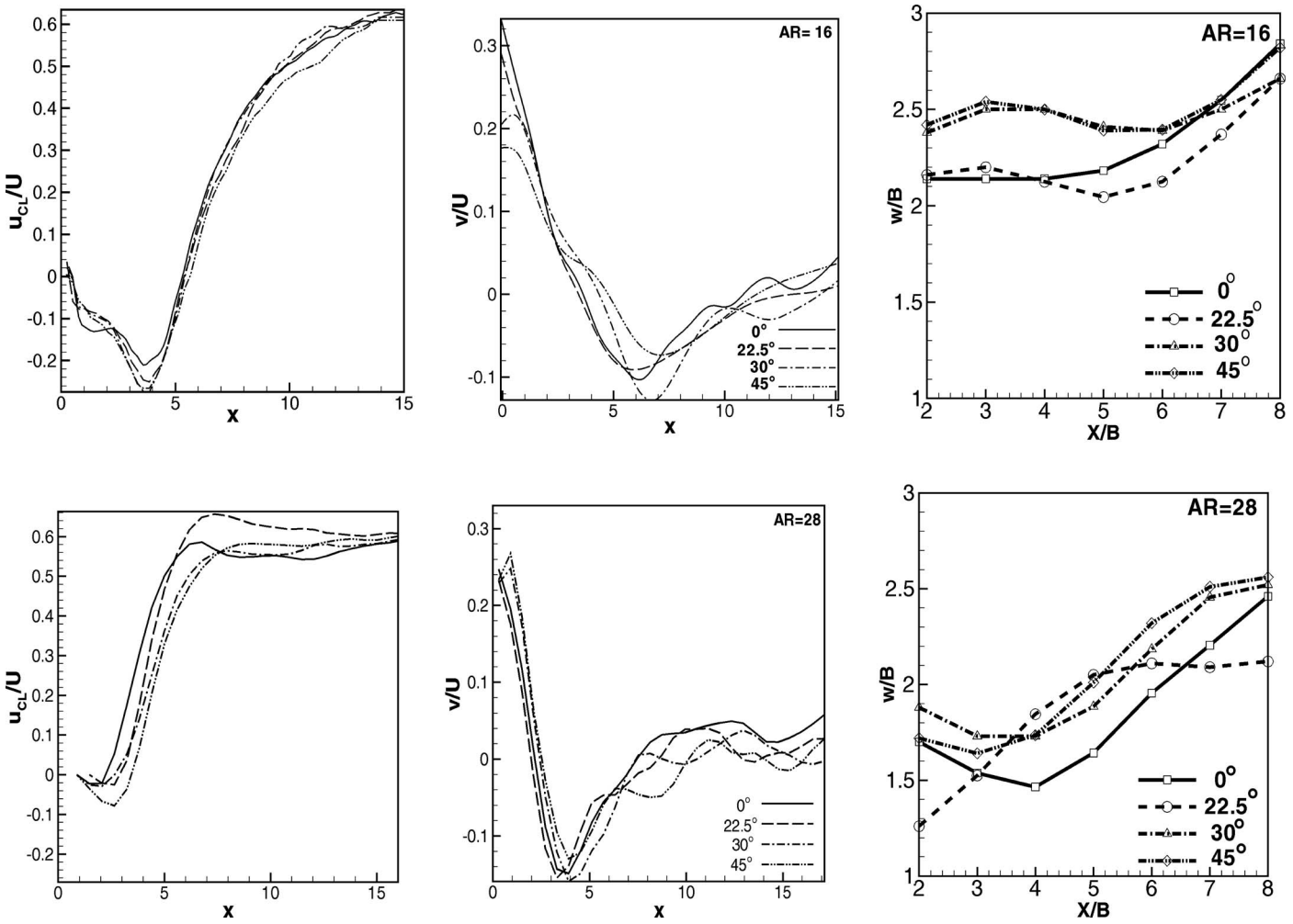

Fig. 10. Centerline recovery of streamwise and transverse velocity component for four cylinder orientations (0, 22.5, 30, and 45°) at two aspect ratios (16 and 28) at R=410. Third column shows wake size for AR=16 and 28.

is in accordance with the larger recirculation bubble for the lower aspect ratio experiment. The greatest negative value attained by the streamwise velocity is higher for AR=16 compared to AR=28. Similarly, the magnitude of the largest transverse velocity is higher for the low aspect ratio cylinder. The average centerline velocity is lower inside the recirculation zone, where the v velocity is high. The minimum in centerline velocity occurs around the core of the recirculation bubble. The streamwise location where v velocity attains a minimum takes place at the end of the recirculation bubble.

Fig. 10 also shows the growth rate of the wake as a function of incidence angle at two different aspect ratios. The wake width (w) is calculated as the cross stream (y) separation of y location corresponding to 50% of velocity deficit, i.e., difference between freestream and minimum velocity. Fig. 10 shows the dependence of wake width on both aspect ratio and cylinder orientation angle. The average wake width is higher at low aspect ratio (AR=16) compared to that at higher aspect ratio (AR=28). Similarly, the wake width is minimal at 22.5° orientation angle in the downstream region. It may be noted that this angle corresponds to minimum drag. The wake reaches an asymptotic state after an initial increase and decrease in its growth rate. The overall wake growth rate can be correlated to the stream trace results of Fig. 8. The wake width increases until the core of the recirculation bubble from downstream of the cylinder and subsequently reduces until the end of the recirculation zone. This is followed by asymptotic increase in wake growth. The smaller recirculation zone size for the AR=28 case in Fig. 8 corresponds to early saturation in growth rate (see Fig. 10).

Time-Averaged Velocity Fluctuation

Fig. 11 compares the total turbulence intensity fields at different cylinder orientations. The streamwise growth of the shear layer shows up in the figure with broadening of the high turbulent zones in the transverse direction. The turbulence intensity is higher for the large aspect ratio cylinder when compared to the low. A greater wall effect along with early onset of three dimensionality for the low aspect ratio cylinder is responsible for dampening the turbulent fluctuations. In addition, the turbulence production is higher for the large aspect ratio cylinder due to the smaller recirculation bubble that leads to a higher velocity gradient in the shear layer. The turbulence intensity increases both in the streamwise and transverse direction from the edge of the cylinder and midplane of the cylinder axis, respectively, with a subsequent drop after reaching a maximum value. The maximum turbulence intensity zone is located at a farther streamwise location for the low aspect ratio when compared to the high. This is in accordance with the larger size of the recirculation bubble for the low aspect ratio cylinder (Fig. 8).

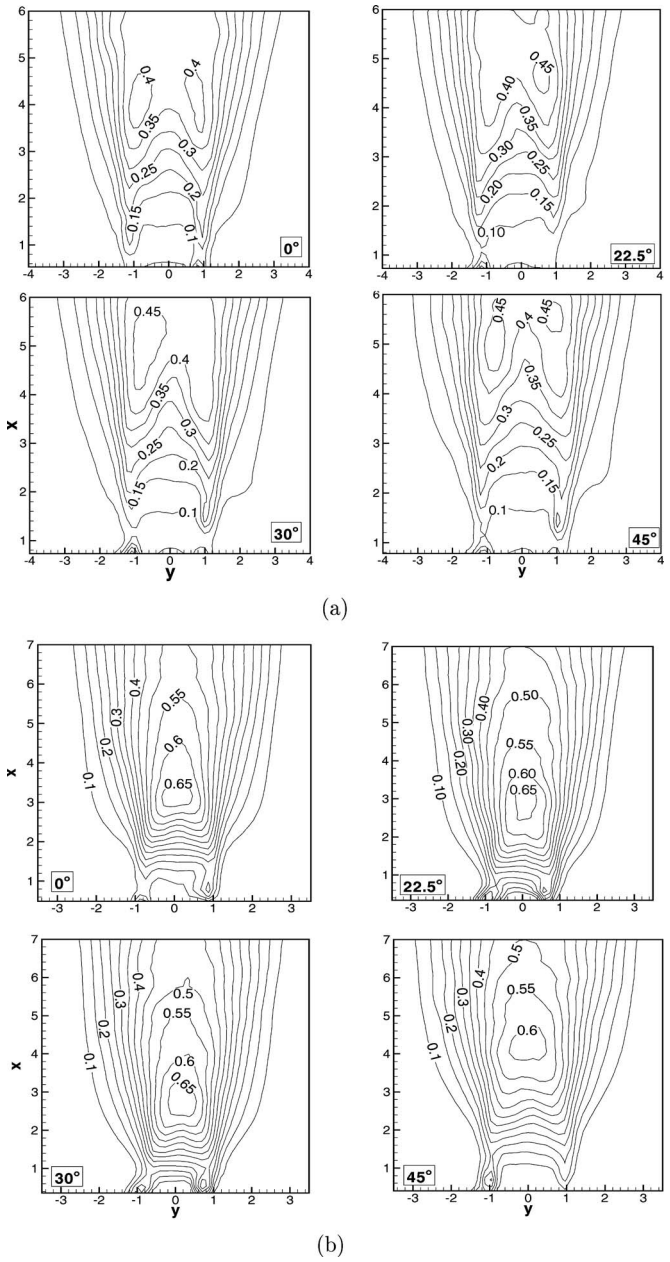

Fig. 11. Contour plot of percentage turbulence intensity $(u_{rms}^2 + v_{rms}^2)^{0.5}/U$ in wake of square cylinder at Reynolds number of 410 for two aspect ratios [16 (a); 28 (b)] and four cylinder orientations. Cylinder center is at $x=0$.

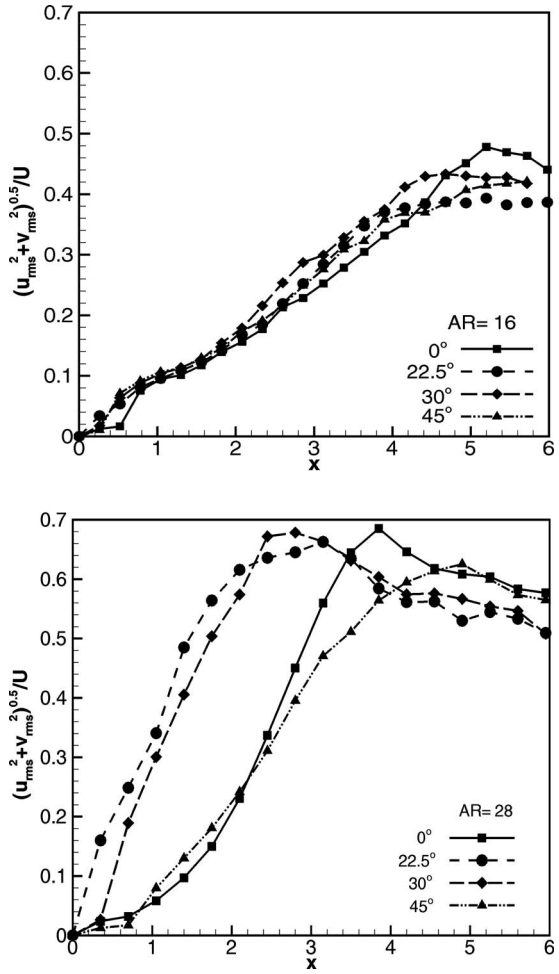

Fig. 12. Turbulence intensity development along centerline for aspect ratios of 16 and 28 at different orientation angle of cylinder

Fig. 12 shows the streamwise variation of the resultant velocity fluctuations at the central midplane ($y=0$) for two aspect ratios (AR=16 and 28) and different cylinder orientations. The objective of this plot is to demonstrate differences in the formation length of the vortices. For both aspect ratios, the turbulence intensity increases in the streamwise direction, reaching a maximum value followed by slow decay. The maximum turbulence intensity appears at a later streamwise location for the lower aspect ratio cylinder. The turbulence intensity for the higher aspect ratio cylinder with orientations of 0 and 45° peaks at a different streamwise location when compared to 22.5 and 30°. This is because at 22.5 and 30°, the flow field is asymmetric when compared to the 0 and 45° angles. For the asymmetric flow field, the turbulence intensity increases faster when compared to the symmetric wake. No significant difference in the turbulence intensity between different incidence angles is observed in the near-field region ($x<2$) of the low aspect ratio cylinder. This is possibly due to the early appearance of three dimensionality (Fig. 7). However, the maximum turbulent intensity continues to be observed slightly earlier for the asymmetric cases of 22.5 and 30° when compared to the symmetric (0 and 45°).

Time-Averaged Vorticity

Spanwise vorticity (namely the vorticity component whose axis is parallel to the cylinder axis) is discussed in the present section. Vorticity values are determined over a grid in terms of circulation per unit area as well as by direct differentiation of the velocity field. The contours plotted on the basis of these two definitions are practically identical. The scale for nondimensionalizing vorticity is U/B.

Fig. 13 shows the contours of time averaged spanwise vorticity (ω_z) at R=410. Contours corresponding to the maximum and minimum values are also shown. The influence of orientation on vorticity can be understood in light of the discussion in the sections "Flow Visualization" and "Time-Averaged Stream Traces."

Fig. 13 shows opposed vorticity of equal strength at both the cylinder corners. The maximum nondimensional value of spanwise vorticity is observed at the cylinder corner, where the shear layer is initiated. In the immediate vicinity of the cylinder, the

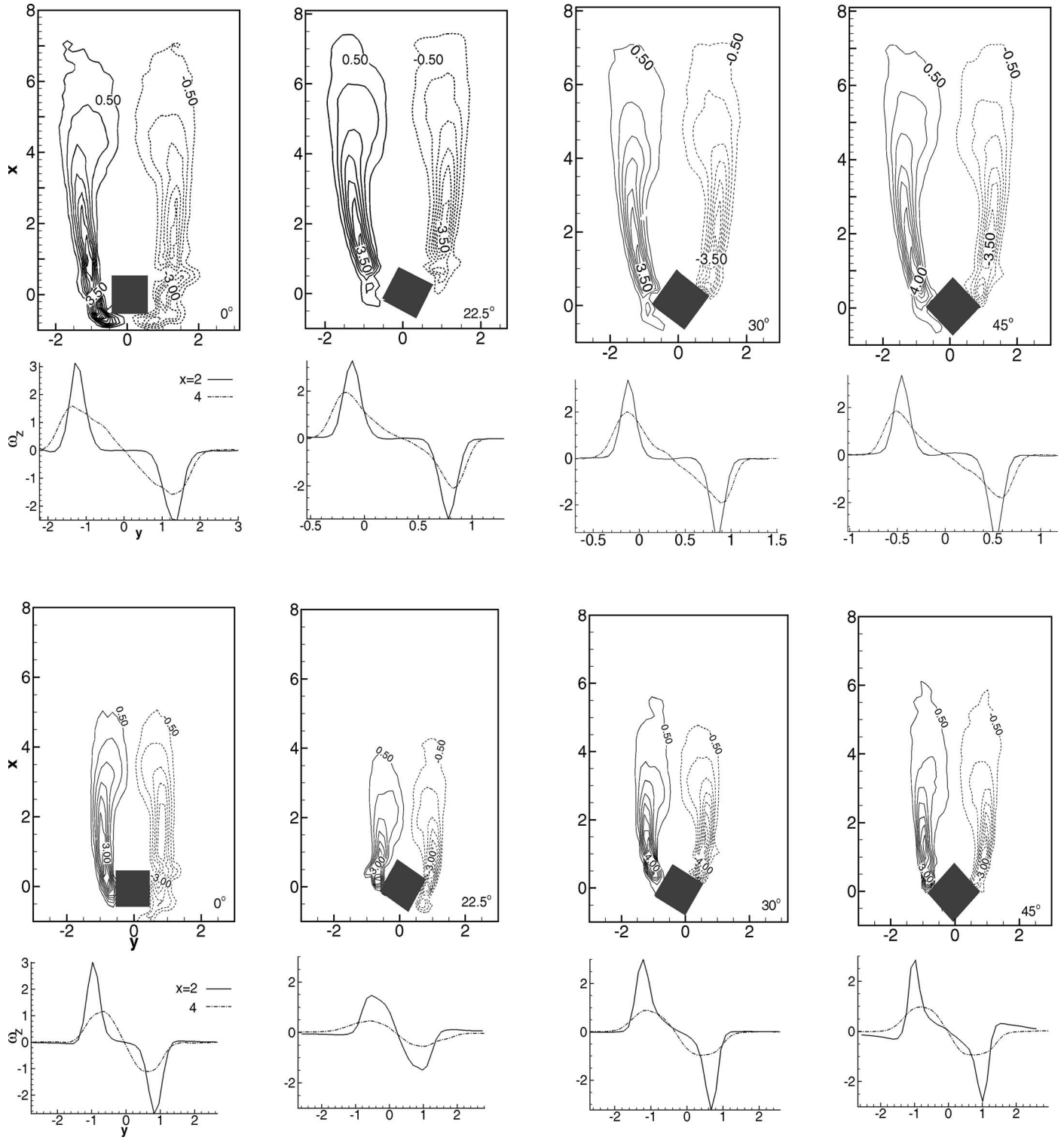

Fig. 13. Time-averaged spanwise vorticity (ω_z) contours for four cylinder orientations and two aspect ratios (16, first row and 28, second row) at R=410. Vorticity profiles are plotted at x=2 and 4. Dashed lines show negative vorticity while solid lines represent positive vorticity; $\Delta\omega_z$=0.5.

vorticity is primarily due to shear in the velocity as the vortices are formed and shed after a certain formation length. The transverse spread of the vortices generated at the corners of the cylinder determines the wake size and is controlled by two opposing factors. First is the lower average pressure within the wake. This is balanced by momentum transport normal to the main flow direction. The latter comprises viscous diffusion along with transport by the time-dependent transverse velocity. These factors lead to a smaller recirculation bubble for the higher aspect ratio cylinder (Fig. 8). Consequently, for a high aspect ratio, the spreading of vortices in the streamwise and transverse directions is smaller when compared to the low aspect ratio cylinder. The peak in the spanwise vorticity component correlates with the minimum in pressure in the near wake, and hence the drag coefficient. Based

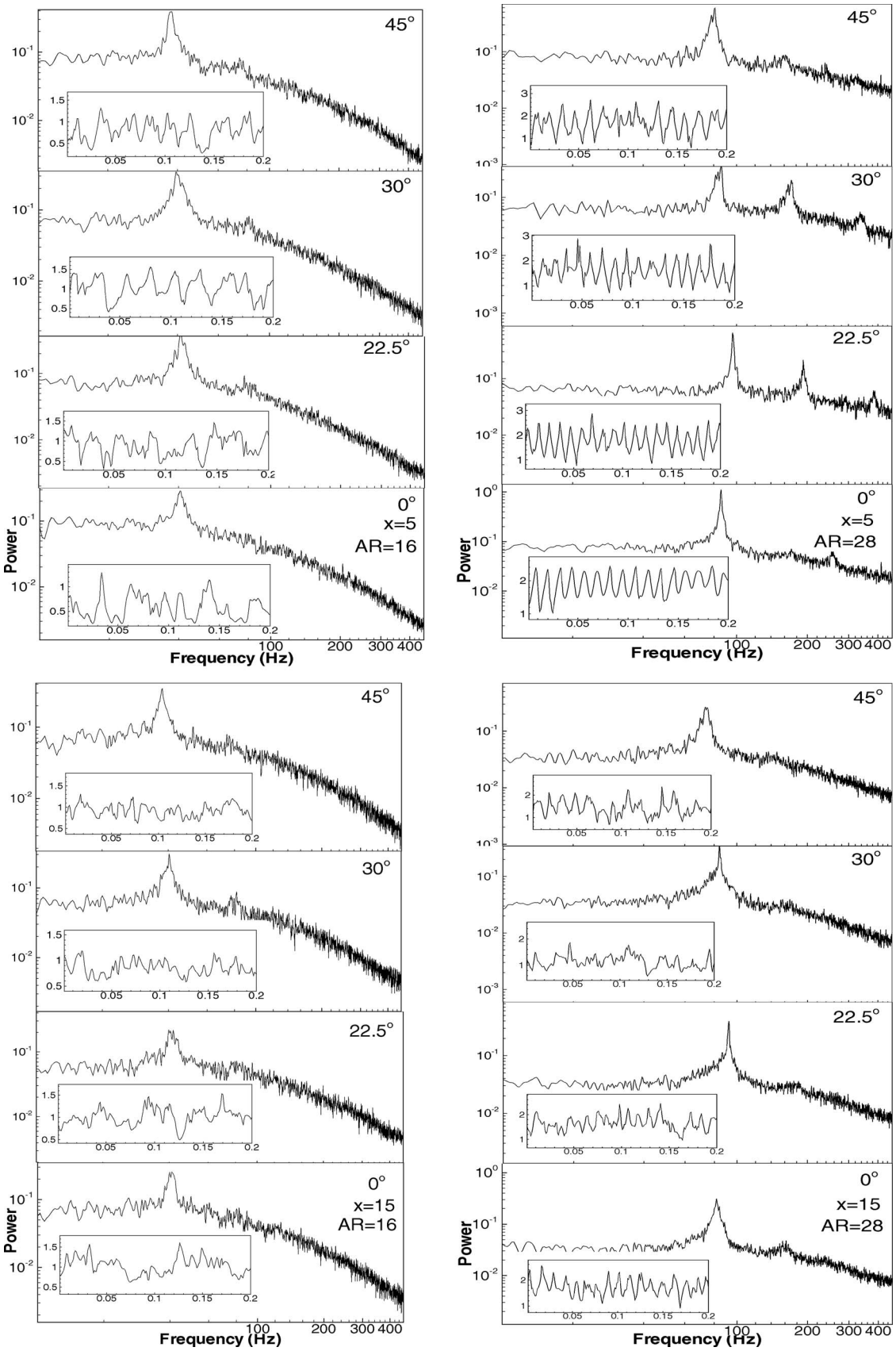

Fig. 14. Power spectra of x component of velocity at R=410 for four different cylinder orientations: x=5, 15; y=1.2; (left) AR=16; (right) AR=28. Inset shows time trace of the transverse component of velocity.

on Fig. 5, higher spanwise vorticity is expected for the lower aspect ratio cylinder. Fig. 13, however, shows that vorticity magnitudes are quite similar for the two aspect ratios. An explanation is the stronger three dimensionality of the flow field for the smaller aspect ratio, that in turns equalizes pressure in the spanwise direction and lowers peak spanwise vorticity values.

Power Spectra

Fig. 14 shows the power spectra of u velocity in the near field ($x=5$) and the far field ($x=15$). The velocity time trace has been inserted in each spectrum plot. The velocity trace confirms the periodic nature of the flow. Spectra were determined by a two-wire hot-wire probe placed at an offset location of $y=1.2$. A clear spectral peak is observed for both low and high aspect ratio cylinders and the peak locations correspond to the vortex shedding frequency. The frequency is higher for AR=28 when compared to AR=16. It confirms the Strouhal number trends reported in Fig. 2. The peak at the vortex shedding frequency is sharper for the high aspect ratio cylinder. The diminished strength at the low aspect ratio is due to a greater quasi-periodicity and jitter in the shedding pattern.

In the near-field region, a second peak is seen for AR=28 at incidence angles equal to 22.5 and 30°. The appearance of these harmonics can be attributed to the nonlinear interaction between the Karman vortices due to flow asymmetry at angles of 22.5 and 30°. The structures of vortices, seen in the flow visualization pictures of Fig. 6, are different for low and high aspect ratio cylinders and support the shapes of the power spectra. The velocity time trace shown as an inset in Fig. 14 also confirms the frequency doubling of the vortex structures. The separation distances between two consecutive shed vortices are different for the high aspect ratio (AR=28) when compared to the low (AR=16). This translates into differing frequency contents in the high aspect ratio experiment.

In the far-field region ($x=15$), the power spectra for AR=28 contain only the fundamental contrary to the presence of an additional harmonics in the near field. The power spectra for higher aspect ratio is less noisy compared to that of the lower aspect ratio in both near and far field regions. The spectra in the inertial subrange have a higher negative slope, closer to $-5/3$, for the low aspect ratio. It confirms an early approach to three dimensionality (Fig. 7).

Conclusions

The effect of orientation of a square cylinder and the role of aspect ratio in determining the wake properties have been experimentally investigated. Particle image velocimetry and hot-wire anemometry have been used for flow measurement. Four cylinder orientations ($\theta=0$, 22.5, 30, and 45°) and two aspect ratios (AR =16 and 28) are studied. The Reynolds number, based on the cylinder size and average upstream velocity, is set equal to 410. Drag coefficient, Strouhal number, centerline recovery, total velocity fluctuations, velocity spectra, stream traces, and vorticity contours are reported. The following conclusions have been arrived at in the present work:

1. A minimum in the time-averaged drag coefficient is seen at 22.5°. At this angle, the Strouhal number is a maximum;
2. The main reason for a minimum in drag coefficient at 22.5° is wake asymmetry originating from shear layers of unequal lengths on each side of the cylinder. The v-velocity profile also bring out the extent of asymmetry in the flow field. The loss of symmetry of the wake increases the transverse velocity, increases the base pressure, and lowers drag. This factor is counterbalanced by an increase in the projected area, but the minimum in the drag coefficient at an orientation of 22.5° reveals that the former has an overall stronger influence at small cylinder angles;
3. Stronger three dimensionality of the flow field at 22.5° additionally contributes to higher base pressure and lower drag;
4. The shorter shear layer on one side of the cylinder governs wake unsteadiness and hence Strouhal number;
5. The visualization images show that the separation distance between the alternating Karman vortices is a function of the cylinder orientation; and
6. Aspect ratio: the size of the recirculation bubble is smaller at the higher aspect ratio. Hence the drag coefficient is correspondingly smaller. At the lower aspect ratio, the shear layers are stabilized, resulting in higher drag and lower Strouhal number. The stronger three dimensionality of flow at the lower aspect ratio has only a marginal overall effect. The turbulence intensity is higher for the larger aspect ratio cylinder since the size of the recirculation size is reduced. Correspondingly, the maximum turbulence intensity appears at an earlier streamwise location. However, the overall dependence of the wake properties on cylinder orientation is seen at both aspect ratios.

Notation

The following symbols are used in this paper:

B = edge of square cylinder (m);
C_D = drag coefficient based on average upstream velocity and B, =drag per unit length/$1/2\rho U^2 B$;
f = dimensionless frequency variable, frequency (Hz) $\times B/U$;
L = length of square cylinder (m);
R = Reynolds number, $\rho UB/\mu$;
S = Strouhal number based on v signal, $f_v B/U$;
U = upstream velocity (m/s);
u = x-component velocity (m/s);
v = y-component velocity (m/s);
w = wake width (m);
X, Y = dimensionless coordinates from cylinder center (m);
x, y = dimensionless coordinates from cylinder center scaled by B. x coordinates is along flow direction;
z = dimensionless coordinates parallel to cylinder axis;
θ = orientation of cylinder with respect to incoming flow;
μ = dynamic viscosity (Pa s);
ρ = fluid density (kg/m^3); and
ω_z = spanwise component of velocity scaled by U/B.

References

Brede, M., Eckelmann, H., and Rockwell, D. (1996). "On secondary vortices in the cylinder wake." *Phys. Fluids*, 8(8), 2117–2123.

Chen, J. M., and Liu, C. H. (1999). "Vortex shedding and surface pressures on a square cylinder at incidence to a uniform air stream." *Int. J. Heat Fluid Flow*, 20, 592–597.

Davis, R. W., Moore, E. F., and Purtell, L. P. (1984). "A numerical-experimental study of confined flow around rectangular cylinders."

Phys. Fluids, 23, 46–59.
Dutta, S., Muralidhar, K., and Panigrahi, P. K. (2003). "Influence of the orientation of a square cylinder on the wake properties." *Exp. Fluids*, 34, 16–23.
Dutta, S., Panigrahi, P. K., and Muralidhar, K. (2007). "Sensitivity of a square cylinder wake to forced oscillations." *J. Fluids Eng.*, 129, 852–870.
Keane, R. D., and Adrian, R. J. (1990). "Optimization of particle image velocimeters. Part I: Double-pulsed system." *Meas. Sci. Technol.*, 1, 1202–1215.
Knisely, C. W. (1990). "Strouhal numbers of rectangular cylinders at incidence: A review and new data." *J. Fluids Struct.*, 4, 371–393.
König, R., Noack, B. R., and Eckelmann, H. (1993). "Discrete shedding modes in the Von Karman vortex street." *Phys. Fluids A*, 5(7), 1846–1848.
Lee, T., and Budwig, R. (1991). "A study of the effect of aspect ratio on vortex shedding behind circular cylinders." *Phys. Fluids A*, 3(2), 309–315.
Li, G. and Humphrey, J. A. C. (1995). "Numerical modelling of confined flow past a cylinder of square cross-section at various orientations." *Int. J. Numer. Methods Fluids*, 20, 1215–1236.
Mansy, H., Yang, P. M., and Williams, D. R. (1994). "Quantitative measurements of three-dimensional structures in the wake of a circular cylinder." *J. Fluid Mech.*, 270, 277–296.
Norberg, C. (1993). "Flow around rectangular cylinders: Pressure forces and wake frequencies." *J. Wind. Eng. Ind. Aerodyn.*, 49, 187–196.
Norberg, C. (1994). "An experimental investigation of the flow around a circular cylinder: Influence of aspect ratio." *J. Fluid Mech.*, 258, 287–316.
Obasaju, E. D. (1983). "An investigation of the effect of incidence on the flow around a square section cylinder." *Aeronaut. Q.*, 34, 243–259.
Okajima, A. (1982). "Strouhal numbers of rectangular cylinders." *J. Fluid Mech.*, 123, 379–398.
Oudheusden, B. W. V., Scarano, F., Hinsberg, N. P. V., and Watt, D. W. (2005). "Phase resolved characterization of vortex shedding in the near wake of a square-section cylinder at incidence." *Exp. Fluids*, 39(1), 86–98.
Panigrahi, P. K., Schroeder, A., and Kompenhans, J. (2005). "PIV investigation of flow behind surface mounted permeable ribs." *Exp. Fluids*, 40, 277–300.
Saha, A. K., Biswas, G., and Muralidhar, K. (2003). "Three-dimensional study of flow past a square cylinder at low Reynolds numbers." *Int. J. Heat Fluid Flow*, 24, 54–66.
Sohankar, A., Norberg, C., and Davidson, L. (1998). "Low-Reynolds-number flow around a square cylinder at incidence: Study of blockage, onset of vortex shedding and outlet boundary condition." *Int. J. Numer. Methods Fluids*, 26, 39–56.
Sohankar, A., Norberg, C., and Davidson, L. (1999). "Simulation of three-dimensional flow around a square cylinder at moderate Reynolds numbers." *Phys. Fluids*, 11(2), 288–306.
Stäger, R., and Eckelmann, H. (1991). "The effect of endplates on the shedding frequency of circular cylinders in the irregular range." *Phys. Fluids A*, 3(9), 2116–2121.
Stansby, P. K. (1974). "The effects of end plates on the base pressure coefficient of a circular cylinder." *Aeronaut. J.*, 87, 36–37.
Szepessy, S., and Bearman, P. W. (1992). "Aspect ratio and end plate effects on vortex shedding from a circular cylinder." *J. Fluid Mech.*, 234, 191–217.
Williamson, C. H. K. (1996). "Vortex dynamics in the cylinder wake." *Annu. Rev. Fluid Mech.*, 28, 477–539.
Williamson, C. H. K. (1997). "Advances in our understanding of vortex dynamics in bluff body wakes." *J. Wind. Eng. Ind. Aerodyn.*, 69–71, 3–32.